Dalton Transactions

PAPER

View Article Online
View Journal | View Issue

Cite this: *Dalton Trans.*, 2014, **43**, 10417

Novel surfactant-free route to delaminated all-silica and titanosilicate zeolites derived from a layered borosilicate MWW precursor†

Xiaoying Ouyang,[a] Ying-Jen Wanglee,[a] Son-Jong Hwang,[b] Dan Xie,[c] Thomas Rea,[c] Stacey I. Zones*[a,c] and Alexander Katz*[a]

Layered borosilicate zeolite precursor ERB-1P (Si/B = 11) is delaminated *via* simultaneous deboronation and SDA removal, to yield material DZ-1 consisting of silanol nests, using a simple aqueous $Zn(NO_3)_2$ treatment. Characterization of this synthesis process by PXRD shows loss of long-range order, and transmission electron microscopy (TEM) demonstrates transformation of rectilinear layers in the layered zeolite precursor to single and curved layers in the delaminated material. N_2 physisorption confirms the expected decrease of micropore volume and increase in external surface area for delaminated materials relative to their calcined 3D zeolite counterpart. Elemental analysis shows loss of B and absence of Zn in the delaminated material. Resonances corresponding to silanol nests are evident *via* ^{29}Si solid-state NMR spectroscopy in DZ-1, which should be located within 12-MR pockets near the external surface. We have successfully utilized these nests as tetrahedral recognition sites for incorporation of Ti within an isolated framework coordination environment in material Ti-DZ-1. Diffuse-reflectance ultraviolet (DR-UV) spectroscopy of Ti-DZ-1 confirms isolated framework Ti sites, which are assigned to bands in the range of 210 nm–230 nm. Infrared spectra of Ti-DZ-1 consist of a distinct absorption band at 960 cm^{-1}, which is absent in DZ-1 prior to Ti incorporation and has been previously correlated with the presence of framework Ti species. Infrared spectra after pyridine adsorption demonstrate bands consistent with Lewis-acid sites in the resulting Ti-substituted delaminated zeolite. The accessibility of these Lewis-acid sites is confirmed when using Ti-DZ-1 as a catalyst for cyclohexene epoxidation using *tert*-butyl hydroperoxide as the organic oxidant – a reaction for which both DZ-1 and TS-1 are inactive.

Received 5th February 2014,
Accepted 19th March 2014

DOI: 10.1039/c4dt00383g

www.rsc.org/dalton

Introduction

Though zeolites exhibit catalytic utility and exquisite levels of shape selectivity due to their well-defined active sites, which consist of framework-substituted heteroatoms, the scope of zeolite catalysis has largely been limited to small reactants that fit inside of micropores, where the majority of active sites are located, within T positions. A growing area of zeolite synthesis involves exposing a larger fraction of active sites, located either on or near the external surface, which offers the potential to impact many areas of catalysis that require accessible and robust sites for larger reactants and products. This has motivated the elegant synthesis and discovery of several types of zeolite-based materials such as extra-large pore zeolites,[1,2] delaminated layered zeolite precursor materials,[3–9] single-unit-cell zeolite nanosheets,[10] hierarchically nanoporous zeolite-like materials,[11,12] and self-pillared zeolite nanosheets.[13] However, all of these synthetic approaches inevitably require an intricate self-assembly between organic surfactants and the inorganic zeolite framework. These surfactants endow the process of accessible zeolite synthesis to be less atom efficient, since they are usually irreversibly consumed by calcination prior to use. Recently, in order to overcome this, there has been great interest and an emergence of approaches for synthesis of accessible zeolitic structures that obviate the need for organic surfactants. We recently reported a single-step delamination method[9] consisting of a simple treatment of a borosilicate layered zeolite precursor ERB-1P (uncalcined material that consists a high amount of piperidine (PI) remaining in the zeolite host lattice, with Si/B = 11) with a warm aqueous $Al(NO_3)_3$ solution at a mild pH of around 3. During delamination, the interlayer hydrogen bonding in the precursor

[a]*Department of Chemical and Biomolecular Engineering, University of California at Berkeley, Berkeley, California 94720, USA. E-mail: SIZO@chevron.com, askatz@berkeley.edu*
[b]*Division of Chemistry and Chemical Engineering, California Institute of Technology, Pasadena, California 91125, USA*
[c]*Chevron Energy Technology Company, Richmond, California 94804, USA*
†Electronic supplementary information (ESI) available. See DOI: 10.1039/c4dt00383g

becomes permanently disrupted (*i.e.*, this disruption persists even after calcination of the material at 550 °C), and is accompanied by isomorphous substitution of Al for B in the framework T-positions. We believe that the permanence of our delamination approach is facilitated by lattice distortions along both the *c*-axis and the *a*–*b* plane, which are induced by substitution of Al for B. Other examples of surfactant-free synthesis of more accessible zeolites include synthesis of MCM-56 analogues,[14–16] IPC-1P,[17] IPC-1PI,[18] IPC-2 and IPC-4.[19]

Synthesis of heteroatom-substituted zeolites where heteroatoms are located in framework T-positions of all-silica analog zeolites is invaluable for zeolite catalysis. Tuning of these heteroatoms and their framework environment within which they reside offers in principle a general method to control active sites, for a variety of different types of catalyzed reactions. Although direct synthesis is a most common way to synthesize heteroatom-substituted zeolites, post-synthesis is often advantageous because it re-inserts heteroatoms into desired T-positions in a more controllable manner, with regard to location within the framework. For example, Chen *et al.* synthesized aluminosilicate zeolites *via* isomorphous substitution of Al for B, where the Al is only re-inserted specifically into 12-MR locations.[20–22] Dartt *et al.* reported the synthesis of large-pore zeolite Ti-SSZ-33, by reacting $TiCl_4$ vapor with deboronated B-SSZ-33 through condensation to release HCl.[23] Wu *et al.* reported the synthesis of a Ti-MWW material by treating deboronated B-MWW with tetrabutyl orthotitanate and amine (*e.g.*, piperidine) under hydrothermal conditions. The as-made Ti-MWW consisted of a significant amount of extraframework Ti species, which were removed *via* nitric-acid wash.[24] All of these post-synthesis methods involve formation of silanol nests, which are formed during deboronation and are subsequently consumed during heteroatom re-insertion. An all-silica zeolite containing a large amount of accessible silanol nests can in principle be employed as a system of tetrahedral binding sites that can subsequently be reoccupied by another metal ion, M, which has a size and oxygen coordination geometry (bond lengths and angles) similar to B in the framework and forms tetrahedral MO_4 sites. To the best of our knowledge, there have not been any reports of the synthesis of an all-silica delaminated zeolite consisting of a high density of silanol nests. Such a material can be useful as a delaminated zeolite platform to afford any type of heteroatom-substituted delaminated zeolite.

Here, in this manuscript, we demonstrate synthesis of an all-silica delaminated zeolite DZ-1, which consists of silanol nests, from a MWW-type layered borosilicate zeolite precursor ERB-1P, as shown in Fig. 1. This new delamination method requires neither organic surfactants, corrosive pH (which can lead to amorphization of the zeolite framework), nor energy-intensive sonication in order to achieve delamination. Our synthesis is accomplished in a single step *via* an extraordinarily simple treatment with a warm $Zn(NO_3)_2$ aqueous solution at a pH of around 1, using a small amount of added HNO_3. The resulting delaminated material consists of a similar topology as previously described ITQ-2 [3] and UCB-1,[5] which also originate from an MWW-type layered zeolite precursor. We also

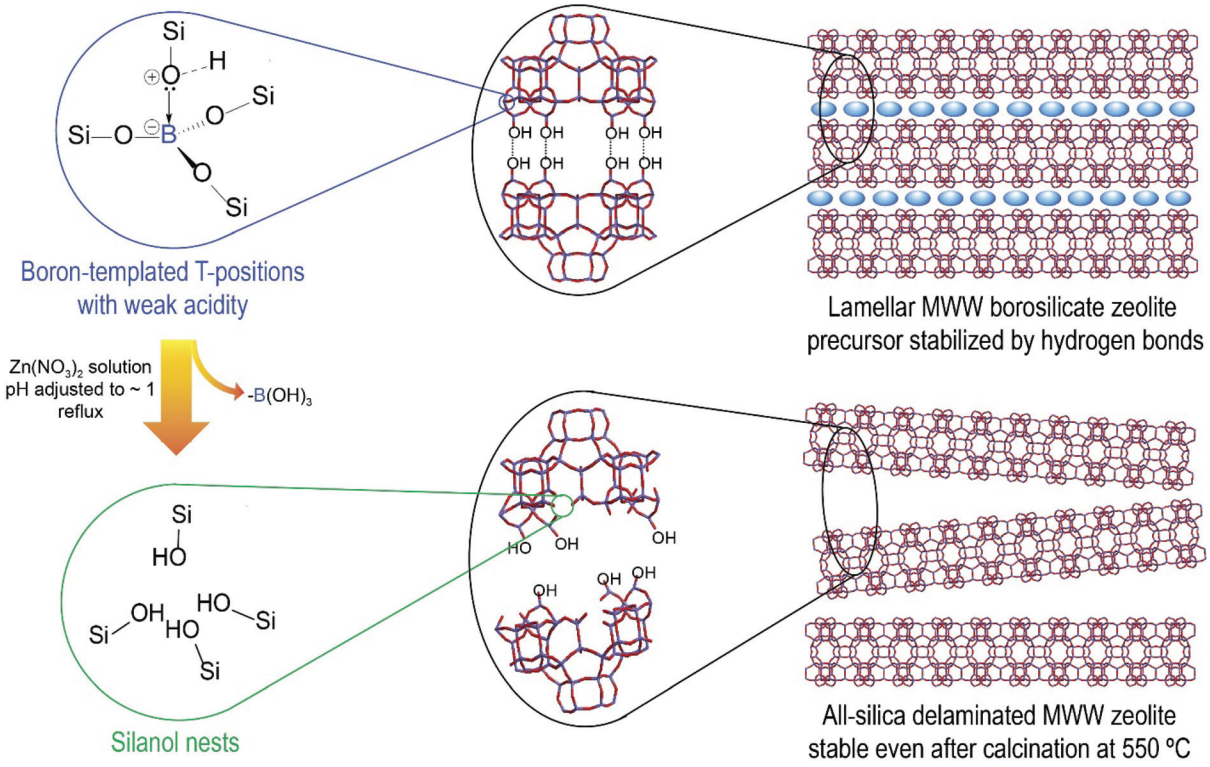

Fig. 1 Schematic diagram of the surfactant-free exfoliation of a MWW-type borosilicate zeolite precursor into a delaminated zeolite consisting high density of silanol nests, and the reoccupation of the silanol nests with various heteroatoms.

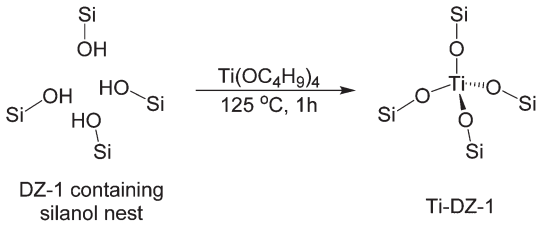

Scheme 1 Ti re-insertion into silanol nest during synthesis of Ti-DZ-1 from DZ-1.

demonstrate reoccupation of the accessible silanol nests located on the external surface of DZ-1 by Ti, to form a delaminated titanosilicate MWW zeolite, which is denoted as Ti-DZ-1 (Scheme 1). The resulting Lewis-acid Ti framework sites are shown to be accessible to large reactants during olefin epoxidation catalysis using a bulky organic hydroperoxide as oxidant.

Experimental section

Materials

All reagents used throughout this manuscript were of reagent-grade quality and were used as-received unless otherwise noted.

Synthesis of ERB-1 precursor (ERB-1P)

Synthesis of ERB-1P was performed based on reported literature procedure, with minor modifications as noted.[25] Typically, 2.40 g of NaOH (EMD Chemicals, 97%) and 6.18 g of H_3BO_3 (≥99.5%, Fisher Chemical) were dissolved in 30 mL of nanopure H_2O, and 12.8 g of PI (≥99.5%, purified by redistillation, Sigma-Aldrich). To this mixture, 9.0 g of SiO_2 (Aerosil® 200, Evonik-Degussa) and 0.10 g of seed crystals (as-made ERB-1P, Si/B = 11) were added. A white viscous gel was obtained after mixing with a spatula. The gel composition in molar ratios was SiO_2 : 0.33 B_2O_3 : 0.2 Na_2O : 1.0 PI : 11.0 H_2O. This gel was subsequently transferred to a 125 mL Parr reactor equipped with a Teflon liner. The reactor was heated at 175 °C for a period of 7–9 days without agitation. After cooling, the contents were poured into a filter, and the precipitated solids were washed several times with water and then air dried.

Synthesis of ERB-1C

The air-dried ERB-1P was first heated at 120 °C for 1 h, then heated to 550 °C at a ramp rate of 1 °C min^{-1}, followed by soaking at 550 °C in air for 5 hours before cooling to room temperature.

Synthesis of DZ-1

In a typical procedure, 1.0 g of zeolite precursor and 4.0 g of $Zn(NO_3)_2{\cdot}6H_2O$ were added to 35 g of pH 1 HNO_3 solution in a 125 mL sealed thick-walled glass reactor, under vigorous stirring. The mixture was heated at 135 °C for 16 h. The resulting delaminated material was denoted as DZ-1. The solid product was collected on a filter, washed thoroughly with water, and finally air-dried.

Synthesis of Ti-DZ-1

In a typical procedure, 4 g of $Ti(OC_4H_9)_4$ was added to 1 g of DZ-1 so as to make a viscous slurry in a sealed, thick-walled glass reactor. The resulting slurry was vigorously stirred for 1 h at 150 °C. Then the temperature was lowered to 120 °C and 20 mL of *n*-BuOH were added to the slurry, followed by additional stirring for 10 min. The solid product was collected on a filter, washed thoroughly with *n*-BuOH so as to remove residual $Ti(OC_4H_9)_4$ and the most weakly-bound Ti species, followed by acetone to remove residual *n*-BuOH, and was finally air-dried. The resulting material was denoted as Ti-DZ-1.

Synthesis of TiO_2/DZ-1

20 mL of $TiCl_4$ solution (1.0 M in toluene, Aldrich) was added to 0.2 g of DZ-1 under dry Ar. The mixture was vigorously stirred at 120 °C for 5 h. The $TiCl_4$-grafted DZ-1 was isolated by decanting the toluene layer in order to remove any unreacted $TiCl_4$, and then dried *in vacuo* to remove any volatile organic solvents. The white solid product was finally calcined in air at 550 °C for 5 hours.

Characterization methods

Powder X-ray diffraction (PXRD) patterns were collected on a Bruker GADDS D-8 diffractometer using a Cu Kα radiation. Data were collected in the 2θ range from 3° to 30° with a step size of 0.02° and a dwell time of 2 s. LeBail-type whole-pattern profile-fitting[26,27] was performed using the GSAS-EXPGUI software package.[28,29] The peak shape function used to fit the powder patterns is the modified Thompson–Cox–Hastings pseudo-Voigt function.[30] Peak asymmetry due to axial divergence was calculated by the model proposed by Finger *et al.*[31]

General

The Si and Al contents of all materials were determined using Inductive Couple Plasma Mass Spectroscopy (ICP-MS) analysis conducted at Galbraith Laboratories, USA. Transmission electron microscopy (TEM) images were recorded on a JEOL JEM-2010 (200 kV) at Chevron Energy Technology Company. Nitrogen physisorption isotherms were measured on a Micromeritics ASAP2020 instrument at 77 K. Prior to measurement, samples were evacuated at 350 °C for 4 h. The pore size distributions were calculated by the non-local density functional (NLDFT) method[32] based on measured nitrogen adsorption data. ^{29}Si solid-state NMR spectroscopy experiments were performed at ambient conditions using a Bruker Avance 500 MHz spectrometer with a wide-bore 11.7 T magnet and employing a 4 mm MAS probe (Bruker). The spectral frequencies were 99.4 MHz for the ^{29}Si nuclei. ^{29}Si CPMAS NMR (CP contact time of 2 ms) and ^{29}Si MAS NMR spectra (after a 4 μs −90° pulse) were acquired with application of a strong ^{1}H decoupling pulse at 8 kHz of sample spinning. The recycle-delay time for the Bloch decay was 300 s. External references were used to calibrate the NMR chemical shifts, and spectra were

reported with reference to tetramethylsilane (TMS) for ^{29}Si nuclei. Infrared spectra of self-supported zeolite pellets were recorded using a Nicolet 6700 FTIR spectrometer at 2 cm^{-1} resolution. Before FTIR experiments, zeolite pellets were first activated at 500 °C *in vacuo* for 2 h. The background spectrum, recorded under identical operating conditions except in the absence of a sample in the cell, was always automatically subtracted from measured spectra. For studying acid sites, the zeolite pellets were exposed to pyridine vapor for approximately 5 min at 25 °C. Spectra were recorded after evacuation for 1 h at 150 °C (3 °C min^{-1} ramp rate from 25 °C).

Catalysis

All chemicals were purchased from Sigma-Aldrich Co. Cyclohexene was purified by passing through a column of Al_2O_3 immediately before use. *n*-Octane was distilled over sodium/benzophenone under Ar. Cyclohexene epoxidation rates and selectivities were measured by using 25 mg of catalyst in a 25 mL flask. 10 mL of anhydrous n-octane, 0.45 mL of cyclohexene, and 1 mL of *tert*-butyl hydroperoxide (TBHP) solution (4.9 mol L^{-1} in nonane, Aldrich) were added to the flask. The reactor was stirred at 60 °C. The concentration of cyclohexene and TBHP in the reaction mixture is 0.40 mol L^{-1} and 0.40 mol L^{-1}, respectively. Liquid aliquots were removed and analyzed for reactants and products by gas chromatography (Agilent 6890, HP-1 methylsilicone capillary column) to measure catalytic reaction rates and selectivities.

Results and discussion

Delamination and Ti re-insertion

Delamination of ERB-1P (Si/B = 11) was performed *via* treatment of the layered borosilicate zeolite precursor with a heated $Zn(NO_3)_2$ aqueous solution at a pH of ~1 under autogenous pressure for 16 h. During this time, interlayer hydrogen bonding in the precursor becomes permanently disrupted (*i.e.*, this disruption persists even after calcination of the material at 550 °C), and is accompanied by loss of framework B due to the acidic condition and extraction of piperidine (PI) by Zn^{2+}. We believe that, similar to our previous $Al(NO_3)_3$-induced delamination method, the permanence of our new delamination approach is facilitated by lattice distortions along both the *c*-axis and the *a*–*b* plane, which are induced by formation of silanol nests as a result of the loss of framework B. The delaminated zeolite DZ-1 has lost the majority of its B (Si/B = 73) and therefore contains a high density of silanol nests. Those silanol nests within the 12-MR located near the external surface should be accessible for heteroatom substitution with metal complexes.

In this study, we attempt to synthesize a delaminated titanosilicate MWW zeolite by reacting a titanium alkoxide precursor with DZ-1. Wu *et al.* demonstrated the synthesis of a delaminated Ti-MWW material by using high pH, organic surfactant, and sonication for exfoliation. The resulting delaminated Ti-BWW consisted of isolated Ti sites throughout the bulk of the material, rather than just near the external surface (*i.e.* within 12-MR).[33] Previously, Dartt *et al.* demonstrated synthesis of Ti-SSZ-33 by reacting $TiCl_4$ vapor with silanol nests.[23] Here, in this manuscript, we chose $Ti(OC_4H_9)_4$ as the Ti-precursor molecule because the relatively lower reactivity of $Ti(OC_4H_9)_4$ towards silanol nests compared with $TiCl_4$ allows the condensation to occur with less formation of extraframework Ti species, as illustrated in Scheme 1. Generally, in this procedure, DZ-1 is added to an excess of $Ti(OC_4H_9)_4$ so as to make a slurry, and stirred at 150 °C for 1 h. The temperature is subsequently lowered to 120 °C, followed by a mild wash consisting of repeated anhydrous *n*-butanol treatments, to wash away unreacted and extraframework $Ti(OC_4H_9)_4$. The *n*-butanol removes surface grafted extraframework Ti species without formation of insoluble TiO_2 precipitate, *i.e.*, $Ti(OSi)(OC_4H_9)_3 + C_4H_9OH \rightarrow Ti(OC_4H_9)_4 + SiOH$.

PXRD characterization

PXRD patterns for the as-made precursor ERB-1P, calcined ERB-1C, all-silica delaminated DZ-1, and Ti-substituted delaminated Ti-DZ-1 materials are shown in Fig. 2. The powder patterns of these materials are indexed on the basis of primitive hexagonal unit cells, as shown in Fig. 2a. Low-angle peaks at 3.19° (reflection (001)) and 6.55° (reflection (002)) represent the layered structure of ERB-1P. Peaks at 7.16° (reflection (100)), and 7.95° (reflection (101)) in pattern (i) in Fig. 2a are consistent with the data previously published for ERB-1P.[25] Similar to previous observations by Millini *et al.*, the intensities of the *c*-axis features, *i.e.*, (001) and (002) reflections, decrease significantly after calcination of ERB-1P at 550 °C in pattern (ii) in Fig. 2. This has been previously attributed to the formation of 10-MR structures between layers, which causes a loss of long-range order along *c*-axis.[25] The (002) reflection shifted from 6.55° in ERB-1P to a value of about 6.97° for ERB-1C, and merged with the (100) reflection at 7.08°, which makes a slightly split peak at around 7.04° for ERB-1C in pattern (ii) in Fig. 2a. Such as shift in the (002) reflection corresponds to a significant contraction of the unit cell, from 26.99 Å in ERB-1P to 24.76 Å in ERB-1C along the *c*-axis, as shown in Table 1. A contraction along the *a*-axis from 14.29 Å in ERB-1P to 14.06 Å in ERB-1C is also observed. Both of these contractions are accompanied by loss of the organic template (PI) during calcination.

Delamination of ERB-1P using the approach described in this manuscript, consisting of deboronation and synthesis of silanol nests, causes loss of long-range order along the *c*-axis and pronounced structural changes in the *a*–*b* plane. This is shown by a comparison of pattern (iii) in Fig. 2a for DZ-1 with that of the calcined material ERB-1C. As in ERB-1C, the (001) reflection for DZ-1 is too weak to be identified. The (002) reflection is at 6.97° in ERB-1C and is 7.20° in DZ-1 in Fig. 2a. The (100) reflection for DZ-1 also exhibits a small but significant shift to lower 2θ angles relative to that for ERB-1C in Fig. 2. The PXRD data of ERB-1P, ERB-1C, DZ-1, and Ti-DZ-1 were analyzed using whole-pattern profile-fitting[26,27] for 2θ = 3–30° (Fig. S1–S4 in ESI†). This fitting demonstrated a contraction of

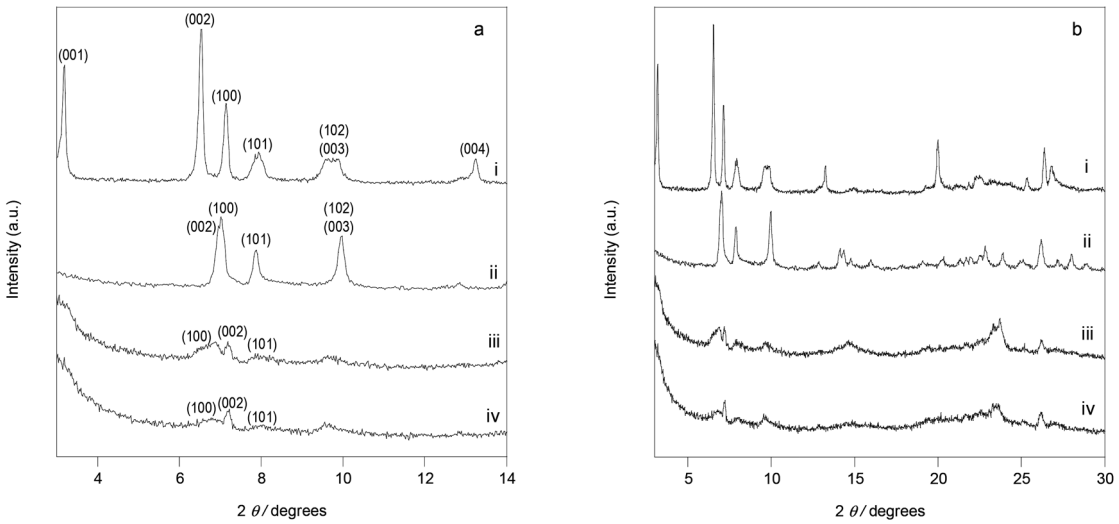

Fig. 2 (a) Indexed PXRD patterns in 2θ = 3–14° exhibiting reflection positions, as obtained from whole-pattern profile-fitting, and (b) PXRD patterns in 2θ = 3–30°, for materials (i) ERB-1P, (ii) ERB-1C, (iii) DZ-1, and (iv) Ti-DZ-1.

Table 1 Unit cell parameters of as-made, calcined, and delaminated ERB-1 materials

Sample ID	Acronym explanation	Treatment	*a* (Å)	*b* (Å)
ERB-1P	ERB-1 precursor	As-made and air-dried	14.29	26.99
ERB-1C	ERB-1 calcined	Directly calcined at 550 °C	14.06	24.76
DZ-1	Delaminated zeolite-1	Delaminated in $Zn(NO_3)_2$ solution (pH = ~1) at 135 °C	14.11	23.76
Ti-DZ-1	Ti re-inserted delaminated zeolite-1	DZ-1 treated with $Ti(OC_4H_9)_4$	14.11	23.76

the unit cell along the *c*-axis, from 24.76 Å to 23.76 Å, and a unit cell expansion of 0.06 Å along the *a*-axis accompanying delamination, when comparing DZ-1 and ERB-1C. The latter expansion is likely caused by the formation of silanol nests which after delamination contain hydrogen bonds at the T-positions, where previously smaller B atoms were condensed before delamination. The PXRD pattern and unit-cell parameters for Ti-DZ-1 are quite similar to DZ-1, probably due to the low Ti concentration in the material (Si/Ti = 67 for Ti-DZ-1).

The sharp peaks for the (101) and (102) reflections in both ERB-1P and ERB-1C are no longer observed in both DZ-1 and Ti-DZ-1, as shown in patterns (iii) and (iv) in Fig. 2a. Instead, a broad band between 8° and 11° due to overlapping (101) and (102) reflections is clearly observed, and the relative intensity of this broad band has been previously used as a metric for evaluating the extent of delamination.[34] In patterns (iii, iv) in Fig. 2a, the (101) and (102) reflections for DZ-1 are much lower in intensity compared with patterns (i) and (ii) for ERB-1P and ERB-1C, respectively, in Fig. 2a. This is consistent with a lack of layer alignment in DZ-1, when using our synthetic delamination approach relying on $Zn(NO_3)_2$ treatment.

Solid-state NMR spectroscopy

^{29}Si MAS and CPMAS NMR spectra shown in Fig. 3 characterize local structure of Si in ERB-1C, DZ-1, and Ti-DZ-1. All spectra in Fig. 3 show the absence of a Q^2 ($\equiv(SiO)_2Si(OH)_2$) resonance, which would otherwise be expected to appear at approximately −80 ppm to −90 ppm.[35] This is strong corroborating evidence that there is no amorphization of the zeolite framework, despite the synthesis of silanol nests (for DZ-1, the amount of silanol nests equals the B content in ERB-1P) as structural defects accompanying delamination during our treatment procedure. A comparison of the ^{29}Si MAS and ^{29}Si CPMAS spectra for each sample demonstrates the presence of silanol-related resonances (*i.e.* the −101 ppm resonance representing Q^3 ($\equiv(SiO)_3$**Si**OH) Si atoms is stronger than resonances centered around −105 ppm representing Q^4 ($\equiv(SiO)_4Si$) Si atoms in the CPMAS spectrum, since CPMAS enhances Q^3 selectively, and this reveals the T-site distribution more efficiently compared with the MAS spectrum). The specific assignments of Q^3 and Q^4 resonances are consistent with results previously reported by Camblor *et al.* for ITQ-1 material[36,37] and are as follows: −94.8 ppm (Q^3), −100.9 ppm (Q^3), −105.2 ppm (Q^4), −110.3 ppm (Q^4), −113.1 ppm (Q^4), −116.5 ppm (Q^4), and −119.5 ppm (Q^4). In our previous study, we showed that delamination results in a significantly sharper Q^3 resonance (−101 ppm) in the ^{29}Si CPMAS NMR spectrum of the Al-exchanged delaminated ERB-1 materials, relative to 3D zeolite ERB-1C, as a result of fewer 10-MR formed due to condensation between layers.[9] For the delaminated materials prepared from the $Zn(NO_3)_2$ route, besides the Q^3 resonance (−101 ppm) due to the uncondensed hydroxyl groups between layers, we also expect another Q^3 resonance due to the hydroxyl groups associated with the silanol nests, which are formed during delamination with $Zn(NO_3)_2$, when most of the framework B (Si/B ratios for ERB-1C and DZ-1 are 10 and 73, respectively) is removed. Indeed, the ^{29}Si CPMAS NMR spectra of DZ-1

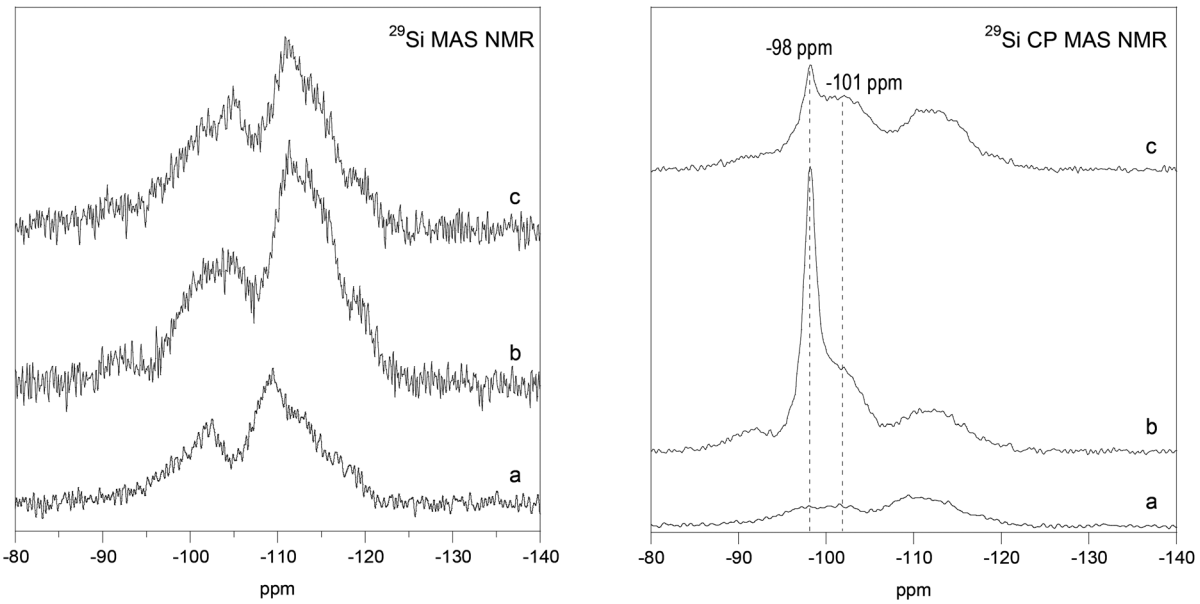

Fig. 3 ^{29}Si MAS and ^{29}Si CPMAS NMR data characterizing (a) ERB-1C (Si/B = 10), (b) DZ-1 (Si/B > 200), and (c) Ti-DZ-1 (Si/Ti = 67).

(Fig. 3b) shows a very sharp resonance at −98 ppm, which is assigned to the Q^3 Si bound to hydroxyls of silanol nests, as well as a shoulder at −101 ppm (ref. 9) for the Q^3 Si bound to uncondensed hydroxyl groups. Both Q^3 resonances (−98 ppm and −101 ppm) are not observed on the ^{29}Si CPMAS NMR spectra of 3D zeolite ERB-1C (Fig. 3a). A similar assignment of the Q^3 resonances for hydroxyl groups associated with silanol nests in zeolite MOR was reported by Wu *et al.*[38]

Ti-DZ-1 is prepared from DZ-1 by reoccupying the silanol nests with tetrahedral Ti sites through condensation of hydroxyls of silanol nests, *i.e.*, $Ti(OC_4H_9)_4$ + 4Si–OH → 4Si–O–Ti + $4C_4H_9OH$. Therefore, we expect to see a lowering intensity of the Q^3 resonances in ^{29}Si CPMAS NMR spectra at −98 ppm for Ti-DZ-1. From Fig. 3c, we can clearly see the Q^3 resonances in the ^{29}Si CPMAS NMR spectrum for Ti-DZ-1. These are much reduced in intensity although not completely absent relative to that for DZ-1 (Fig. 3b), which suggests that Ti has been successfully incorporated in some of the accessible near-surface silanol nests, to synthesize framework Ti atoms. This reduction in the Q^3 resonance at −98 ppm for the Ti-DZ-1 sample relative to the as-made DZ-1 sample suggests that Ti is most likely located in isolated framework T-positions. However, due to the bulky size of $Ti(OC_4H_9)_4$, the heteroatoms are only able to access near-surface silanol nests, and are not able to penetrate into the 10-MR channels and thereby condense to all internal silanol nests.

TEM characterization

TEM images of ERB-1P show the expected lamellar assembly consisting of rectilinear sheets in Fig. 4(c), whereas in comparison images of the delaminated zeolite DZ-1 in Fig. 4(a) clearly show curved thin layers that lack long-range order, which is consistent with PXRD data in Fig. 2. Consistent with data from N_2 physisorption in Fig. 5 and Table 2, such a highly delaminated morphology is still well preserved after reoccupation of silanol nests with Ti, as shown in Fig. 4(b) for Ti-DZ-1.

N_2 physisorption at 77 K

N_2 adsorption–desorption isotherms of ERB-1C, DZ-1, and Ti-DZ-1 were measured for textural characterization, and are shown in Fig. 5a, with the pore-size distributions derived from the NLDFT model[32] illustrated in Fig. 5a (and S6 of ESI†). Table 2 lists micropore and mesopore volumes, as well as external surface areas, as determined by the *t*-plot method. The N_2 physisorption data for DZ-1 is consistent with success in delamination as discussed and shown using PXRD (Fig. 2) and TEM (Fig. 4a). The external surface area of DZ-1 is 2.5-fold higher than that of the corresponding calcined 3D zeolite ERB-1C. DZ-1 also exhibits significantly lower micropore volume and higher mesopore volume due to delamination, relative to ERB-1C. Ti-DZ-1 is prepared from DZ-1 where the silanol nests in the 12-MR surface pockets of DZ-1 are reoccupied by tetrahedral Ti. N_2 physisorption shows the preservation of a delaminated morphology in Ti-DZ-1, which is consistent with the results from TEM characterization in Fig. 4b. Compared to DZ-1, Ti-DZ-1 shows a decreased micropore volume (0.04 $cm^3\ g^{-1}$ for Ti-DZ-1 *vs.* 0.08 $cm^3\ g^{-1}$ for DZ-1), increased mesopore volume (0.14 $cm^3\ g^{-1}$ for Ti-DZ-1 *vs.* 0.10 $cm^3\ g^{-1}$ for DZ-1), and increased external surface area (171 $m^2\ g^{-1}$ Ti-DZ-1 *vs.* 131 $m^2\ g^{-1}$ for DZ-1). If such micropore-volume reduction in Ti-DZ-1 relative to DZ-1 was due to pore blockage by any extraframework Ti species, greater mesopore volume as well as larger external surface area would not be observed. Therefore, we attribute this micropore-volume reduction and increase in mesopore volume/external surface area to further layer separation, as promoted by the incorporation of Ti into silanol nests within DZ-1. Results from B elemental analysis demonstrate that more than 80% of the B is removed during delamination.

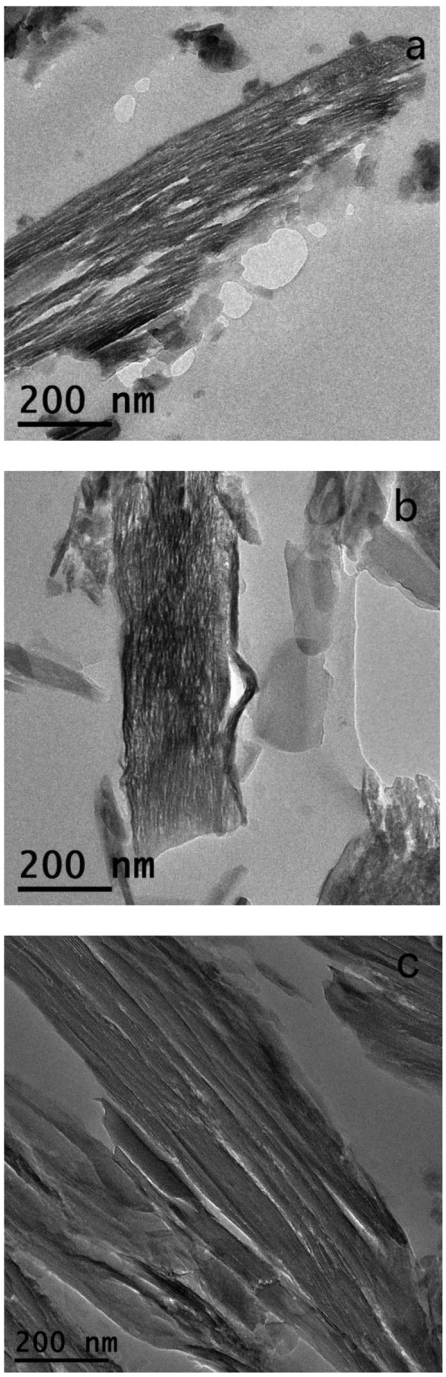

Fig. 4 TEM images characterizing (a) DZ-1, (b) Ti-DZ-1, and (c) ERB-1P.

Assuming reasonably that each removed B synthesizes a silanol nest, the ratio of Si atoms to silanol nests is estimated to be 10 : 1 in DZ-1 following delamination. Such a large amount of silanol nests as structural defects could cause the delaminated zeolite sheets to become mechanically less strong and more likely to partially collapse. Once the structural defects (or silanol nests) are healed by condensation of Ti into these framework positions, the delaminated zeolite sheets have the mechanical integrity required to support better layer separation without collapse. Similar observations were reported in our previous study, where we found that calcined ERB-1P that had been deboronated *via* acid treatment yields a material with more than two-fold lower external surface area than the directly calcined ERB-1P. This was attributed to partial collapse of the ERB-1 structure, as presumably caused by the formation of a high density of silanol nests.[9]

Solid-state diffuse-reflectance ultraviolet (DR-UV) spectroscopy

For Ti heteroatoms located in a silicate framework, there are distinct charge transfer transitions involving framework oxygen anions and framework Ti cations. Such transitions are usually located in the UV region, and have a higher energy of the corresponding absorption band upon lowering the Ti coordination number (or, equivalently, increasing the degree of coordinative unsaturation of Ti). For instance, TS-1 has exclusively isolated tetrahedral framework Ti, and its DR-UV absorption band consists of a sharp peak centered at 210 nm assigned to O→Ti charge-transfer (CT) band.[39] However, the absorption band for anatase, which is the aggregated form of TiO_2 consisting of octahedral Ti sites, is more broad and is located around 330 nm.[40] We performed DR-UV spectroscopy to investigate the coordination environment of Ti within DZ-1, as shown in Fig. 6. The DR-UV spectrum of Ti-DZ-1 consists of bands within the range of 210–230 nm. These bands have been previously assigned to isolated Ti sites in the TS-1 framework as well as in MCM-41, which have a coordination number of either four or six (attributed to water coordination).[41,42] TiO_2/DZ-1 (Ti: 2.2 wt%, Si/Ti = 29) (prepared using $TiCl_4$ rather than $Ti(OC_4H_9)_4$) is also studied as a comparison material. The DR-UV spectrum for TiO_2/DZ-1 shows a broad absorption band centered at 247 nm for extraframework Ti sites,[39] in addition to a shoulder at 330 nm for anatase, as shown in Fig. 6a. This data suggests that Ti-DZ-1 is more similar to Ti-MCM-41 rather than TiO_2/DZ-1.

FTIR spectroscopic characterization

FTIR spectroscopy has been previously employed as an important tool for characterizing Ti-containing zeolites. For example, in the 400–1500 cm^{-1} range of the IR spectrum for TS-1, there is a distinct band located at 960 cm^{-1}, but this 960 cm^{-1} band is almost negligible in Silicate-1.[43] While the precise origin of the 960 cm^{-1} band in Ti-containing materials remains under some debate, some reports correlate the appearance of the 960 cm^{-1} band and an increase in unit-cell volume as Ti is incorporated into the framework,[44,45] while other studies reveal that this band can also be due to a Si–O framework vibration.[46,47] It therefore seems reasonable that the 960 cm^{-1} band is a necessary but insufficient characterization of Ti-containing materials,[48] since even some non-Ti-containing Beta zeolites are also reported to have 960 cm^{-1} band.[43] We clearly see that intensity of the 960 cm^{-1} band is negligible for DZ-1 (Fig. 7a), but, in stark contrast, this band is strong for Ti-DZ-1 (Fig. 7b), which is very similar to what has been reported for Silicate-1 and TS-1.[43] Therefore, the presence of the 960 cm^{-1} band in Ti-DZ-1 supports that Ti is incorporated into the

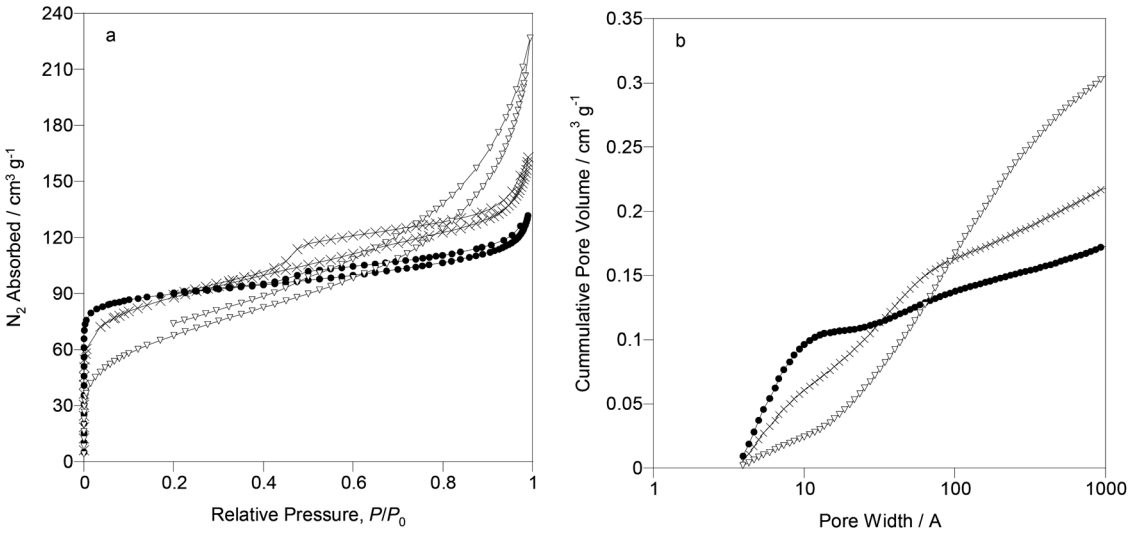

Fig. 5 (a) N_2 adsorption isotherms and (b) N_2 NLDFT cumulative pore volume plots for ERB-1C (●), calcined DZ-1 (×), and calcined Ti-DZ-1 (▽).

Table 2 Synthesis conditions and physicochemical properties of DZ-1 related materials

Sample[a]	Heteroatom (M)	Metal precursor	Si/M ratio	Si/B ratio	V_{micro}[c] (cm^3 g^{-1})	V_{meso}[d] (cm^3 g^{-1})	S_{ext}[e] (m^2 g^{-1})
ERB-1C	B	n/a	n/a	10	0.12	0.04	53
DZ-1	n/a	$Zn(NO_3)_2$	n/a[b]	73	0.08	0.10	131
Ti-DZ-1	Ti	$Ti(OC_4H_9)_4$	67	73	0.04	0.14	171

[a] All the samples in Table 2 are calcined materials. [b] The Si/Zn ratio for DZ-1 is >200. [c] Micropore volume determined by *t*-plot method. [d] Mesopore (between 1 and 10 nm in diameter) volume determined by NLDFT method. [e] External surface area determined by *t*-plot method.

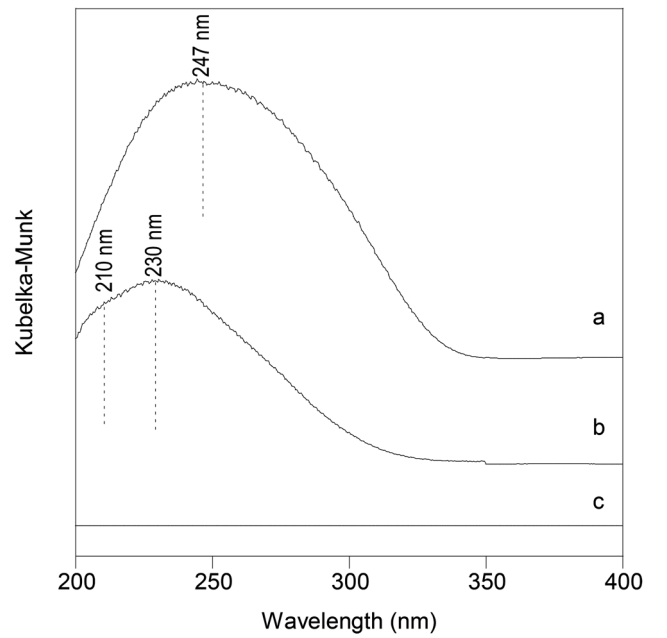

Fig. 6 DR-UV data characterizing (a) TiO_2/DZ-1, (b) Ti-DZ-1, and (c) DZ-1.

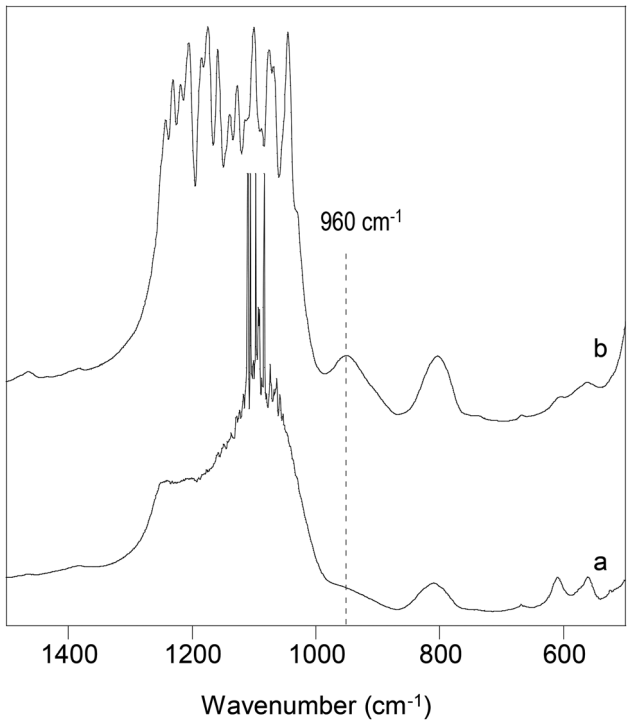

Fig. 7 FT-IR spectra of (a) DZ-1 and (b) Ti-DZ-1.

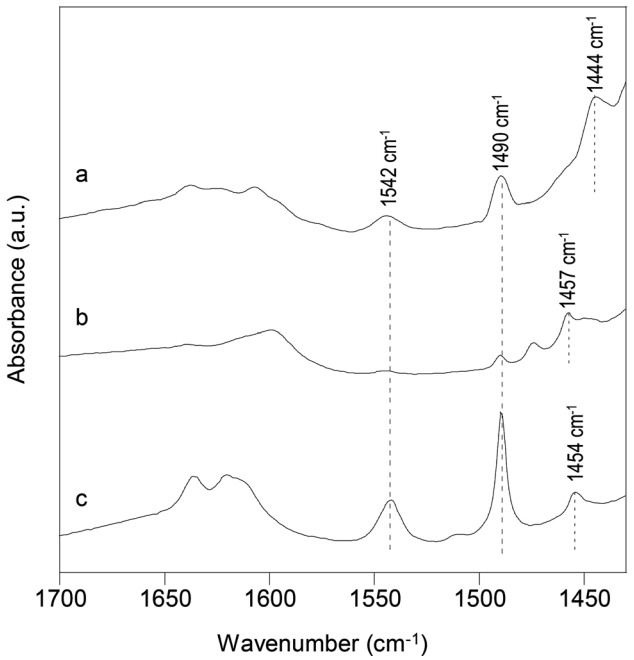

Fig. 8 FTIR spectra of activated samples, (a) Ti-DZ-1, (b) DZ-1, and (c) ERB-1-del-135, recorded after pyridine adsorption at 25 °C and desorption at 150 °C.

zeolite framework, and is not located within an extraframework environment such as anatase.

Characterization of acid sites by pyridine adsorption

The relative amount and strength of acid sites of the as-made DZ-1 and Ti-DZ-1 are compared with ERB-1-del-135, which is a delaminated aluminosilicate ERB-1 material (Si/Al = 15, S_{ext} = 133 m^2 g^{-1}, V_{micro} = 0.09 cm^3 g^{-1}),[9] by means of FTIR spectroscopy of the pyridine adsorbed at room temperature followed by desorption at 150 °C. The FTIR spectra in the window of 1700–1430 cm^{-1} are shown in Fig. 8. Infrared bands at 1542 cm^{-1} and 1454 cm^{-1} correspond to pyridine bound to Brønsted-acid sites (PyH^+) and Lewis-acid sites (PyL), respectively, and are clearly observed for ERB-1-del-135. As expected, the 1542 cm^{-1} PyH^+ band for DZ-1 and Ti-DZ-1 is weak, and its residual intensity at 1542 cm^{-1} is most likely due to the small amount of B (Si/B = 73) residing in the framework of DZ-1 and Ti-DZ-1. A weak band at 1457 cm^{-1} is observed for DZ-1. This is assigned to residual framework B, since such a band has been previously observed by Corma *et al.* and ascribed to Lewis acid sites formed by framework B sites in B-Beta.[49] Ti-DZ-1 exhibits a small shoulder at 1457 cm^{-1} for the Lewis-acid sites due to residual framework B, but it also contains a much stronger peak located at 1444 cm^{-1} due to framework-Ti Lewis-acid sites. A similar band located at around 1444 cm^{-1} has been previously assigned to Lewis-acid sites in TS-1.[50]

Epoxidation catalysis of cyclohexene with TBHP

We confirmed the accessibility and catalytic activity of Ti Lewis-acid sites using the epoxidation of cyclohexene *tert*-butyl hydroperoxide (TBHP) in the liquid phase as a model reaction. Our approach to investigate the Lewis-acid sites of Ti-DZ-1 for catalysis was comparative in nature and used both DZ-1 and TS-1 as additional catalysts. This reaction is shown in Scheme 2 and was chosen because it provides direct information about the external acid-site accessibility and catalytic activity, since olefin epoxidation with TBHP can only be catalyzed by Lewis acid sites, and this reaction should only occur on the external surface due to the steric bulk of the reactants, for all catalysts investigated. Catalysis data on the epoxidation of cyclohexene with TBHP over Ti-DZ-1, DZ-1, and TS-1 are summarized in Table 3. The TON for Ti-DZ-1 (TON = 262) is significantly higher than DZ-1 (TON = 0) and TS-1 (TON ≈ 0). Such a result can be rationalized by the fact that DZ-1 is a Ti-free sample, and the 10-MR system within TS-1 is too restrictive from the standpoint of shape selectivity to allow either bulky cyclohexene or TBHP access to internal Ti sites. Altogether, based on solid-state DR-UV and FTIR spectroscopies as well as catalysis data, Ti re-insertion in all-silica DZ-1 leads to isolated Lewis-acid sites, which are active for olefin epoxidation catalysis, and these Lewis acid sites are very accessible for bulky substrates, since they are located at the external surface.

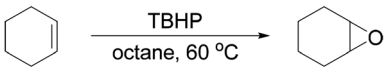

Scheme 2 Chemical equation of epoxidation of cyclohexene with TBHP.

Table 3 Epoxidation of cyclohexene with TBHP catalyzed by various zeolite catalysts[a]

Sample	Si/Ti ratio	Conversion (%) (mol epoxide mol^{-1} initial TBHP)	Epoxide selectivity (%)	TON (mol epoxide mol^{-1} Ti)
Ti-DZ-1	67	8.1	82	262
DZ-1	∞	0	n/a	0
TS-1	80	~0.1	n/a[b]	0

[a] Reaction condition: 25 mg of zeolite catalyst, 0.40 mol L^{-1} TBHP, 0.40 mol L^{-1} cyclohexene, 10 mL octane as solvent, 60 °C, 2 h. [b] The yield of epoxide is too low to calculate the selectivity to epoxide product.

Comparative synthetic studies of delamination

We recently demonstrated that both framework B and a neutral pore filler (rather than a quaternary ammonium structure-directing agent) are necessary attributes for delaminating layered borosilicate zeolite precursors, when using our synthetic method consisting of isomorphous substitution with $Al(NO_3)_3$ solution.[9] The $Zn(NO_3)_2$-induced delamination method described within this manuscript shares some similarities with this previous $Al(NO_3)_3$-based delamination method. Both the current and previously described methods remove framework B and PI organic template. However, the crucial differ-

ence is that $Al(NO_3)_3$ leads to isomorphous substitution of larger Al for smaller B, which facilitates delamination due to lattice distortion, whereas $Zn(NO_3)_2$ does not lead to isomorphous substitution because Zn^{2+} is too unstable to occupy a zeolite framework position under the hydrothermal conditions (135 °C) of delamination. The consequence of this instability is the synthesis of silanol nests as structural defects during B loss, which also helps to preserve the delaminated zeolite sheets due to lattice distortion. Therefore, we expect similar requirements as in the previous method, with regards to both framework B and a neutral pore filler being required for the $Zn(NO_3)_2$-induced delamination reported in this manuscript. We further compare $Zn(NO_3)_2$- and $Al(NO_3)_2$-based delamination methods below.

First, there are two roles for $Zn(NO_3)_2$ treatment during the delamination process. The first of these is that Zn cations are known to form complexes with N-containing ligands,[51–53] such as amines and amides, which makes the $Zn(NO_3)_2$ play a role as a scavenger for PI organic template removal *via* its coordination to the N lone electron pairs. Second, aqueous $Zn(NO_3)_2$ solution consists of bulky hydrated $Zn(H_2O)_6^{2+}$ cations, which may disrupt the interlayer hydrogen bonding between sheets in the layered zeolite precursor. Such similar effects of hydrogen bond disruption have also been attributed to $Al(H_2O)_6^{2+}$ cations in our previous $Al(NO_3)_3$-based delamination.[9] To explore the requirement of $Zn(H_2O)_6^{2+}$ cations on delamination, we treated ERB-1P in acid only, such as dilute HNO_3 solution (pH = 1) either at 135 °C or room temperature, as well as 50 wt% acetic acid (pH = 1.5) at 135 °C. As summarized in Table 4, none of these Zn-free syntheses exhibit any delamination. Instead, there is even a decrease in external-surface area, probably due to partial collapse of the three-dimensional zeolite structure, as caused by the loss of framework B without reoccupying these T-positions with other heteroatoms, when performing these acid-only treatments. Therefore, $Zn(H_2O)_6^{2+}$ has an essential role in the delamination approach described in this manuscript.

Next, we explore the role of acidic conditions. Unlike $Al(NO_3)_3$ solution, which has a pH of ~3.5 in our previously described $Al(NO_3)_3$-based delamination method, the pH of $Zn(NO_3)_2$ solution is ~5.5. To understand whether it is necessary to conduct delamination with $Zn(NO_3)_2$ under more acidic conditions, we treated ERB-1P with both neutral and acidic $Zn(NO_3)_2$ solutions, which have pH values of 5.5 and 1, respectively. The pH 1 $Zn(NO_3)_2$ solution was prepared by adding HNO_3 to an existing $Zn(NO_3)_2$ solution. The results in Table 4 show that the treatment with acidic $Zn(NO_3)_2$ led to a successful delaminated DZ-1, which has a decreased micropore volume and an increased external surface area relative to the 3D zeolite ERB-1C (V_{mico}: 0.08 $cm^3\ g^{-1}$ for DZ-1 *vs.* 0.12 $cm^3\ g^{-1}$ for ERB-1C; S_{ext}: 131 $m^2\ g^{-1}$ for DZ-1 *vs.* 53 $m^2\ g^{-1}$ for ERB-1C). The results from the treatment with neutral $Zn(NO_3)_2$ demonstrated a lower micropore volume of only 0.02 $cm^3\ g^{-1}$, while its external surface area was only slightly increased to 68 $m^2\ g^{-1}$. Such a severe 6-fold decrease in micropore volume and only a 1.3-fold increase in external surface area relative to the three-dimensional ERB-1C zeolite suggests that delamination is most likely hindered by severe pore blockage. A likely source of the pore blockage is the precipitation of insoluble zinc salt, such as zinc borate, which may form during reaction between zinc salt and boric acid. Boric acid can be easily formed when a borosilicate (*e.g.* ERB-1P) is deboronated under hydrothermal conditions.[54] Furthermore, results from ICP analysis show that DZ-1 synthesized with acidic $Zn(NO_3)_2$ has a negligible amount of Zn (~95 ppm) in the final product, whereas the failed DZ-1 synthesized with neutral $Zn(NO_3)_2$ has a large amount of Zn (10.4 wt%) present in the sample. Finally, we found that treatment with both acidic $Zn(NO_3)_2$ and neutral $Zn(NO_3)_2$ led to removal of PI organic template at the same level of ~50%, as shown by the results from TGA in Fig. S6 and S7.† This supports our hypothesis that $Zn(H_2O)_6^{2+}$ acts as a scavenger of PI removal. Therefore, we propose that a sufficiently strong acidic condition is required in order to prevent from pore blockage by precipitated Zn salts and promote delamination by keeping the Zn soluble and available to complex with PI structure-directing agent.

We subsequently attempted delamination with acidic $Zn(NO_3)_2$ solution on several other layered zeolite precursors and silicates, including MCM-22P,[55] Na-kanemite,[56] B-SSZ-25,[57] and B-SSZ-70.[58,59] We considered two factors when choosing these reference materials. First, we wished to investigate the importance of whether the presence of B in the zeolite framework is crucial to delamination. Second, we chose materials so as to vary the types of organic templates, which can be either used as a pore filler, when used as a small neutral amine, or as a structure-directing agent, when used as a bulky quaternary SDA. MCM-22P has no B in its framework, but it has HMI as the pore filler, which is very similar to the role of PI in ERB-1P. Thus, this comparison can be used to investigate whether B is required for delamination. On the other hand, B-SSZ-25 and B-SSZ-70 both have B in their framework, but their organic templates are bulky quaternary ammonium salts. Therefore, a comparison of ERB-1P with B-SSZ-25 and B-SSZ-70 was used to better understand the role of organics in the delamination. Finally, Na-kanemite was used because it has neither B nor organic templates.

Results of our attempts for delaminating the aforementioned layered zeolite precursors are listed in Table 4. There was no increase in external surface area for B-SSZ-25 and B-SSZ-70 after treating with $Zn(NO_3)_2$ solution (Table 4). The SDAs for B-SSZ-25 and B-SSZ-70 syntheses were sterically bulky quaternized amines, and we found no removal of these SDAs upon attempting delamination under our conditions, using TGA analysis. Such results are consistent with results on delamination of B-SSZ-25 and B-SSZ-70 when using the previously reported $Al(NO_3)_3$-based method.[9] The possible reason may be that these SDAs are impossible to extract *via* protonation or metal complex formation and remain too tightly bound inside of the zeolite cages due to their larger size. Thus, we believe that when using the delamination method described in this manuscript, a relatively small and neutral pore filler is also required for delamination. Although MCM-22P has a pore

Table 4 Comparative studies of delamination[a] of various layered zeolite precursors

Samples	SDA	Reagent	Si/Al ratio	Si/B ratio	3D zeolite		After delamination	
					V_{micro} ($cm^3\ g^{-1}$)	S_{ext}[d] ($m^2\ g^{-1}$)	V_{micro} ($cm^3\ g^{-1}$)	S_{ext}[d] ($m^2\ g^{-1}$)
ERB-1P	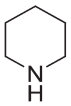	Acidic $Zn(NO_3)_2$[b]	n/a	11	0.12	53	0.08	131
		Neutral $Zn(NO_3)_2$[c]					0.02	68
		$Al(NO_3)_3$					0.09	133
		HNO_3[e]					0.04	10
		HNO_3 (r.t.)[f]					0.15	25
		HAc[g]					0.10	20
MCM-22P	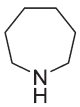	Acidic $Zn(NO_3)_2$[b]	27	n/a	0.14	56	0.12	53
		$Al(NO_3)_3$					0.12	55
Na-kanemite	n/a	Acidic $Zn(NO_3)_2$[b]	n/a	n/a	0	6	0	6
		$Al(NO_3)_3$					0	6
B-SSZ-25	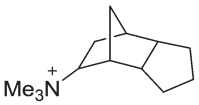	Acidic $Zn(NO_3)_2$[b]	n/a	35	0.13	30	0.12	28
		$Al(NO_3)_3$[h]					0.11	23
B-SSZ-70	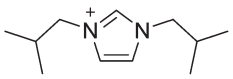	Acidic $Zn(NO_3)_2$[b]	n/a	30	0.18	54	0.18	46
		$Al(NO_3)_3$[h]					0.18	55

[a] The delamination was conducted on 200 mg of each zeolite precursor in 0.4 N $Al(NO_3)_3$ solution at 135 °C for 1 d. The resulting materials were calcined in air at 550 °C for 5 h to remove SDAs. [b] The pH of $Zn(NO_3)_2$ solution was adjusted to 1 by adding HNO_3. [c] No HNO_3 is added to the $Zn(NO_3)_2$, pH = 5.5. [d] External surface area determined by *t*-plot method. [e] 200 mg of ERB-1P was treated with HNO_3 solution, pH = 1, at 135 °C for 1 d, and then calcined in air at 550 °C for 5 h. [f] Same as [e], except that the treatment was conducted at room temperature for 1 d. [g] 200 mg of ERB-1P was treated with 50 wt% HAc solution, pH = 1.5, at 135 °C for 1 d, and then calcined in air at 550 °C for 5 h. [h] The Al content is negligible (≈200 ppm).

filler very similar to that of ERB-1P, its delamination was also unsuccessful, evidenced by no increase in external surface area (Table 4). This result suggests that B is required in the layered zeolite precursor and that only removal of some organic SDA does not lead to delamination. The attempt to delaminate Na-kanemite with the approach described within this manuscript was also unsuccessful. This can be rationalized on the basis of lack of both framework B and organic template as pore filler.

Conclusions

In this work, we report a surfactant-free synthesis of delaminated all-silica MWW zeolite, which is prepared by heating a MWW borosilicate zeolite precursor, ERB-1P, in zinc nitrate solution (pH adjusted to ~1). During this treatment, powder X-ray diffraction (PXRD) shows a complete loss of long-range order, and transmission electron microscopy (TEM) shows loss of rectilinear microstructure and formation of curved thin layers. N_2 physisorption shows a consistent increase in external surface accompanying delamination, represented by a factor of 2.5-fold. This new delamination method is facilitated by the removal of B and PI organic template from the zeolite structure, while no heteroatom is re-inserted and a high density of silanol nests are formed. These silanol nests are present as structural defects which cause lattice distortion and lead to the preservation of the delaminated zeolitic layers. The existence of the silanol nests is evidenced by ^{29}Si MAS and CPMAS NMR spectroscopy, where a very sharp Q^3 peak located at −98 ppm in DZ-1 can be assigned to the hydroxyl groups of silanol nests. Upon Ti re-insertion, this Q^3 peak at −98 ppm diminished significantly due to the reoccupation of silanol nests by tetrahedral Ti.

Ti is re-inserted into the silanol nests within DZ-1 by condensing $Ti(OC_4H_9)_4$ with release of *n*-butanol. Diffuse-reflectance UV spectroscopy shows absorption bands in the range of 210–230 nm in Ti-DZ-1, which is consistent with isolated framework Ti sites having a coordination number between 4 and 6 (attributed to water coordination). IR spectra of Ti-DZ-1 show a distinct band at 960 cm^{-1}, but the Ti-free DZ-1 doesn't have any noticeable band at 960 cm^{-1}. Such similar consequence of Ti incorporation in zeolite framework has been observed for TS-1. Pyridine adsorption of Ti-DZ-1 investigated by IR spectroscopy shows that Ti sites likely have Lewis acid properties. The catalytic activity for epoxidation of cyclohexene with TBHP over Ti-DZ-1 further confirms the Lewis acid properties. Finally, comparative synthetic studies of the $Zn(NO_3)_2$-induced delamination process employing related MWWF layered zeolite precursors demonstrate that framework B, a neutral pore filler (rather than a quaternary ammonium structure-directing agent), and acidic condition (*e.g.*, pH ~ 1) are required.

Acknowledgements

The authors are grateful to the Management and Transfer of Hydrogen *via* Catalysis Program funded by Chevron Corporation. The NMR facility at Caltech was supported by the

National Science Foundation under Grant Number 9724240 and partially supported by the MRSEC Program of the NSF under Award Number DMR-520565. X.O. is also grateful of Dr. Cong-Yan Chen of Chevron Corporation for providing Na-kanemite.

References

1 M. E. Davis, *Chem. – Eur. J.*, 1997, **3**, 1745–1750.
2 J. Jiang, J. Yu and A. Corma, *Angew. Chem., Int. Ed.*, 2010, **49**, 3120–3145.
3 A. Corma, V. Fornés, S. B. Pergher, T. L. M. Maesen and J. G. Buglass, *Nature*, 1998, **396**, 353–356.
4 S. Maheshwari, E. Jordan, S. Kumar, F. S. Bates, R. L. Penn, D. F. Shantz and M. Tsapatsis, *J. Am. Chem. Soc.*, 2008, **130**, 1507–1516.
5 I. Ogino, M. M. Nigra, S.-J. Hwang, J.-M. Ha, T. Rea, S. I. Zones and A. Katz, *J. Am. Chem. Soc.*, 2011, **133**, 3288–3291.
6 E. A. Eilertsen, I. Ogino, S.-J. Hwang, T. Rea, S. Yeh, S. I. Zones and A. Katz, *Chem. Mater.*, 2011, **23**, 5404–5408.
7 W. J. Roth and J. Čejka, *Catal. Sci. Technol.*, 2011, **1**, 43–53.
8 I. Ogino, E. A. Eilertsen, S.-J. Hwang, T. Rea, D. Xie, X. Y. Ouyang, S. I. Zones and A. Katz, *Chem. Mater.*, 2013, **25**, 1502–1509.
9 X. Ouyang, S.-J. Hwang, R. C. Runnebaum, D. Xie, Y.-J. Wanglee, T. Rea, S. I. Zones and A. Katz, *J. Am. Chem. Soc.*, 2013, **136**, 1449–1461.
10 M. Choi, K. Na, J. Kim, Y. Sakamoto, O. Terasaki and R. Ryoo, *Nature*, 2009, **461**, 246–U120.
11 W. Fan, M. A. Snyder, S. Kumar, P.-S. Lee, W. C. Yoo, A. V. McCormick, R. L. Penn, A. Stein and M. Tsapatsis, *Nat. Mater.*, 2008, **7**, 984–991.
12 K. Na, C. Jo, J. Kim, K. Cho, J. Jung, Y. Seo, R. J. Messinger, B. F. Chmelka and R. Ryoo, *Science*, 2011, **333**, 328–332.
13 X. Zhang, D. Liu, D. Xu, S. Asahina, K. A. Cychosz, K. V. Agrawal, Y. Al Wahedi, A. Bhan, S. Al Hashimi, O. Terasaki, M. Thommes and M. Tsapatsis, *Science*, 2012, **336**, 1684–1687.
14 L. Wang, Y. Wang, Y. Liu, L. Chen, S. Cheng, G. Gao, M. He and P. Wu, *Microporous Mesoporous Mater.*, 2008, **113**, 435–444.
15 Y. Wang, Y. Liu, L. Wang, H. Wu, X. Li, M. He and P. Wu, *J. Phys. Chem. C*, 2009, **113**, 18753–18760.
16 G. Liu, J.-G. Jiang, B. Yang, X. Fang, H. Xu, H. Peng, L. Xu, Y. Liu and P. Wu, *Microporous Mesoporous Mater.*, 2013, **165**, 210–218.
17 W. J. Roth, O. V. Shvets, M. Shamzhy, P. Chlubná, M. Kubu, P. Nachtigall and J. Čejka, *J. Am. Chem. Soc.*, 2011, **133**, 6130–6133.
18 P. Chlubná, W. J. Roth, H. F. Greer, W. Zhou, O. Shvets, A. Zukal, J. Čejka and R. E. Morris, *Chem. Mater.*, 2013, **25**, 542–547.
19 W. J. Roth, P. Nachtigall, R. E. Morris, P. S. Wheatley, V. R. Seymour, S. E. Ashbrook, P. Chlubná, L. Grajciar, M. Položij, A. Zukal, O. Shvets and J. Čejka, *Nat. Chem.*, 2013, **5**, 628–633.
20 C. Y. Chen and S. I. Zones, in *13th International Zeolite Conference*, ed. A. Galarneau, F. Di Renzo, F. Fujula and J. Vedrine, Elsevier, Amsterdam, 2001, p 11-P-16.
21 C. Y. Chen and S. I. Zones, in *13th International Zeolite Conference*, ed. A. Galarneau, F. Di Renzo, F. Fujula and J. Vedrine, Elsevier, Amsterdam, 2001, p 26-O-05.
22 C. Y. Chen and S. I. Zones, *U.S. Patent*, 6,468,501 B1, 2002.
23 C. B. Dartt and M. E. Davis, *Appl. Catal., A*, 1996, **143**, 53–73.
24 P. Wu and T. Tatsumi, *Chem. Commun.*, 2002, 1026–1027.
25 R. Millini, G. Perego, W. O. Parker, G. Bellussi and L. Carluccio, *Microporous Mater.*, 1995, **4**, 221–230.
26 A. Le Bail, H. Duroy and J. L. Fourquet, *Mater. Res. Bull.*, 1988, **23**, 447–452.
27 A. Le Bail, *Powder Diffr.*, 2005, **20**, 316–326.
28 A. C. Larson and R. B. Von Dreele, Los Alamos National Laboratory Report LAUR, 2000, 86-748.
29 B. H. Toby, *J. Appl. Crystallogr.*, 2001, **34**, 210–213.
30 P. Thompson, D. E. Cox and J. B. Hastings, *J. Appl. Crystallogr.*, 1987, **20**, 79–83.
31 L. W. Finger, D. E. Cox and A. P. Jephcoat, *J. Appl. Crystallogr.*, 1994, **27**, 892–900.
32 P. I. Ravikovitch, G. L. Haller and A. V. Neimark, *Adv. Colloid Interface Sci.*, 1998, **76**, 203–226.
33 P. Wu, D. Nuntasri, J. Ruan, Y. Liu, M. He, W. Fan, O. Terasaki and T. Tatsumi, *J. Phys. Chem. B*, 2004, **108**, 19126–19131.
34 W. J. Roth and D. L. Dorset, *Microporous Mesoporous Mater.*, 2011, **142**, 32–36.
35 E. Lippmaa, M. Maegi, A. Samoson, G. Engelhardt and A. R. Grimmer, *J. Am. Chem. Soc.*, 1980, **102**, 4889–4893.
36 M. A. Camblor, C. Corell, A. Corma, M. J. Díaz-Cabañas, S. Nicolopoulos, J. M. González-Calbet and M. Vallet-Regí, *Chem. Mater.*, 1996, **8**, 2415–2417.
37 M. A. Camblor, A. Corma, M. J. Díaz-Cabañas and C. Baerlocher, *J. Phys. Chem. B*, 1998, **102**, 44–51.
38 P. Wu, T. Komatsu and T. Yashima, *J. Phys. Chem.*, 1995, **99**, 10923–10931.
39 P. Ratnasamy, D. Srinivas and H. Knozinger, in *Advances in Catalysis*, ed. B. C. Gates and H. Knozinger, 2004, vol. 48, pp. 1–169.
40 B. Notari, in *Advances in Catalysis*, ed. D. D. Eley, W. O. Haag and B. Gates, Academic Press, 1996, vol. 41, pp. 253–334.
41 F. Geobaldo, S. Bordiga, A. Zecchina, E. Giamello, G. Leofanti and G. Petrini, *Catal. Lett.*, 1992, **16**, 109–115.
42 A. Corma, M. T. Navarro and J. P. Pariente, *J. Chem. Soc., Chem. Commun.*, 1994, 147–148.
43 C. B. Dartt, C. B. Khouw, H. X. Li and M. E. Davis, *Microporous Mater.*, 1994, **2**, 425–437.
44 D. R. C. Huybrechts, P. L. Buskens and P. A. Jacobs, *J. Mol. Catal.*, 1992, **71**, 129–147.

45 A. J. H. P. van der Pol, A. J. Verduyn and J. H. C. van Hooff, *Appl. Catal., A*, 1992, **92**, 113–130.
46 M. R. Boccuti, K. M. Rao, A. Zecchina, G. Leofanti and G. Petrini, in *Structure and Reactivity of Surfaces*, ed. C. Morterra, A. Zecchina and G. Costa, Elsevier, Amsterdam, 1989, p. 133.
47 A. Zecchina, G. Spoto, S. Bordiga, A. Ferrero, G. Petrini, G. Leofanti and M. Padovan, in *Zeolite Chemistry and Catalysis*, Elsevier, Amsterdam, 1991, p. 251.
48 D. R. C. Huybrechts, I. Vaesen, H. X. Li and P. A. Jacobs, *Catal. Lett.*, 1991, **8**, 237–244.
49 A. Corma, M. E. Domine and S. Valencia, *J. Catal.*, 2003, **215**, 294–304.
50 F. Bonino, A. Damin, S. Bordiga, C. Lamberti and A. Zecchina, *Langmuir*, 2003, **19**, 2155–2161.
51 M. Uchiyama, Y. Matsumoto, D. Nobuto, T. Furuyama, K. Yamaguchi and K. Morokuma, *J. Am. Chem. Soc.*, 2006, **128**, 8748–8750.
52 J. Qian, W. Gu, H. Liu, F. Gao, L. Feng, S. Yan, D. Liao and P. Cheng, *Dalton Trans.*, 2007, 1060–1066.
53 Z. Dai, X. Xu and J. W. Canary, *Chem. Commun.*, 2002, 1414–1415.
54 S. I. Zones, A. Benin, S.-J. Hwang, D. Xie, S. Elomari and M.-F. Hsieh, *J. Am. Chem. Soc.*, 2014, **136**, 1462–1471.
55 M. E. Leonowicz, J. A. Lawton, S. L. Lawton and M. K. Rubin, *Science*, 1994, **264**, 1910–1913.
56 C. Y. Chen, S. Q. Xiao and M. E. Davis, *Microporous Mater.*, 1995, **4**, 1–20.
57 S. I. Zones and S.-J. Hwang, *Microporous Mesoporous Mater.*, 2011, **146**, 48–56.
58 R. H. Archer, S. I. Zones and M. E. Davis, *Microporous Mesoporous Mater.*, 2010, **130**, 255–265.
59 R. H. Archer, J. R. Carpenter, S.-J. Hwang, A. W. Burton, C.-Y. Chen, S. I. Zones and M. E. Davis, *Chem. Mater.*, 2010, **22**, 2563–2572.